ACS APPLIED MATERIALS & INTERFACES

Research Article

www.acsami.org

Bioinspired Peptide Nanostructures for Organic Field-Effect Transistors

Thiago Cipriano,[†] Grant Knotts,[‡] Amrit Laudari,[‡] Roberta C. Bianchi,[†] Wendel A. Alves,*[,†] and Suchismita Guha*[,‡]

[†]Centro de Ciências Naturais e Humanas, Universidade Federal do ABC, 09210-580, Santo André, São Paulo, Brazil

[‡]Department of Physics and Astronomy, University of Missouri, Columbia, Missouri 65211, United States

Supporting Information

ABSTRACT: Peptide-based nanostructures derived from natural amino acids are superior building blocks for biocompatible devices as they can be used in a bottom-up process without the need for expensive lithography. A dense nanostructured network of L,L-diphenylalanine (FF) was synthesized using the solid−vapor-phase technique. Formation of the nanostructures and structure−phase relationship were investigated by electron microscopy and Raman scattering. Thin films of L,L-diphenylalanine micro/nanostructures (FF-MNSs) were used as the dielectric layer in pentacene-based field-effect transistors (FETs) and metal−insulator−semiconductor diodes both in bottom-gate and in top-gate structures. Bias stress studies show that FF-MNS-based pentacene FETs are more resistant to degradation than pentacene FETs using FF thin film (without any nanostructures) as the dielectric layer when both are subjected to sustained electric fields. Furthermore, it is demonstrated that the FF-MNSs can be functionalized for detection of enzyme−analyte interactions. This work opens up a novel and facile route toward scalable organic electronics using peptide nanostructures as scaffolding and as a platform for biosensing.

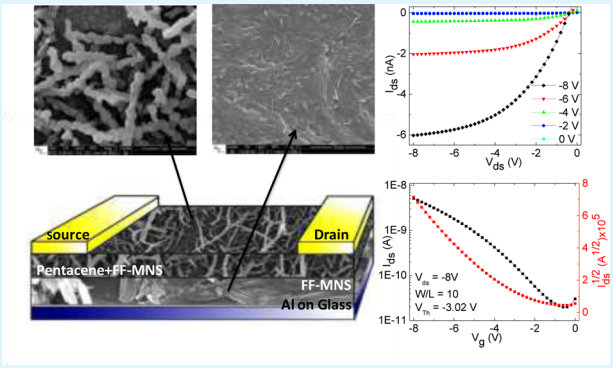

KEYWORDS: *field-effect transistors, peptide nanostructures, pentacene, electrochemical impedance spectroscopy*

1. INTRODUCTION

The nanostructures obtained from biomolecules are attractive due to their biocompatibility, ability for molecular recognition, and ease of chemical modification. Peptide-based self-assemblies derived from natural amino acids are superior building blocks for biocompatible and other devices as they can be used in a bottom-up process without any need for expensive lithography.[1−4] By mimicking the structures occurring in nature, peptide materials play a unique role in a new generation of hybrid materials. Phenylalanine-containing polypeptides have amphiphilic properties that help in their self-assembly and result in a variety of well-defined structures, such as nanorods, nanotubes, and nanospheres.[5,6] Such molecular self-assemblies are a result of various inter/intramolecular interactions: van der Waals, electrostatic, and hydrogen bonds. The self-assembly mechanism further depends on the preparation conditions, such as concentration, pH, and temperature.[7,8] Additionally, due to the ease of manipulating peptide nanostructures on various substrates for active materials, one can conjure up new functionalities in electronic devices.

The L,L-diphenylalanine micro/nanostructures (FF-MNSs) have good thermal and chemical stability.[5] The solid−vapor-phase synthesis results in a dense network of horizontal FF-MNSs on different substrates. Such a network not only provides scaffolding for other active materials but also enhances the substrate surface area that may be used for applications in sensors, transistors, and solar cells. Another unique property of peptide nanostructures is their ferroelectric nature,[1,9,10] which may be induced by annealing at high temperatures. The polar hexagonal form of FF-MNSs is known to show an irreversible phase transition at ∼140 °C to a nonpolar orthorhombic structure.[11]

Organic field-effect transistors (OFETs) are being actively developed for applications in large-area flexible electronics.[12,13] A requirement for such applications is that both the active semiconducting layer and the gate dielectric layer be solution processable. Getting away from oxide dielectrics, such as SiO_2 and Al_2O_3, in OFETs not only is cost effective but has tremendous advantages for improving carrier mobility and stability of devices.[14] Much effort has gone into modification of the dielectric interface; appropriate gate dielectrics that are free of electron-trapping groups, such as hydroxyl or silanol, have allowed the demonstration of *n*-channel OFETs,[15] which is otherwise not observable with oxide dielectrics. In order to

Received: September 17, 2014
Accepted: November 7, 2014
Published: November 7, 2014

achieve stable and low-operating voltage OFETs, the dielectric surface should be hydrophobic and must provide a relatively high capacitance, which is often a challenge with many polymer dielectrics because they have an inherently low dielectric constant. Thus, other strategies involving solvent manipulation have been used.[16,17]

Peptide nanostructures pave the way for a novel class of dielectrics in both bottom-gate and top-gate OFET architectures, with applications in biosensing and piezoelectric devices. Top-gate OFETs with polymer dielectrics are often a challenge with low-cost spin-coating techniques, since the solvents used for dissolving the polymer dielectric degrades the underlying organic semiconductor layer. The solvents used for dispersing peptide nanostructures are usually orthogonal to the organic semiconducting layer and thus provide a simple fabrication route toward top-gate OFETs. The hydrophilic and hydrophobic nature of the surface of FF-MNS can be controlled by changing their phase. It was recently shown that the surface of hypercin-conjugated FF-MNSs in the hexagonal phase is more hydrophobic than the surface of the orthorhombic phase.[6,18] The high surface area and hydrophobic nature of the hexagonal phase of FF-MNSs provide a superior organic molecular/polymer-dielectric interface.

In this work we demonstrate pentacene OFETs using FF-MNSs as the dielectric layer in both bottom- and top-gate geometries. The FF-MNSs were synthesized using a solid−vapor-phase strategy and either spin coated or drop casted to form thin films. The nanostructures were characterized using scanning electron microscopy and Raman scattering. OFETs, metal insulator semiconductor (MIS) diodes, and metal insulator metal (MIM) capacitors utilizing FF-MNSs were electrically characterized. The p-type charge carrier mobilities of pentacene OFETs were $\sim 10^{-2}-10^{-3}$ cm^2 V^{-1} s^{-1}, and the bottom-gate devices operated at voltages lower than 10 V. Preparing the FF-MNSs in the orthorhombic phase did not significantly improve OFET performance over hexagonal phase FF-MNSs. Interestingly, FF-MNSs also allow for straightforward top-gate pentacene OFET architecture, which is usually a challenge with most polymer dielectrics due to solvent incompatibility issues with pentacene. Furthermore, we show that FF-MNSs may be functionalized for detecting enzyme−analyte interaction using electrochemical methods. This work is the first demonstration of the application of FF-MNSs in active organic electronics and opens up many avenues for a new generation of biocompatible materials for 21st century electronics.

2. EXPERIMENTAL METHODS

2.1. Materials. All reagents used were of analytical grade. Sulfuric acid, absolute ethanol, methanol, potassium dihydrogen phosphate, and urea were purchased from Synth (Brazil). Aniline, 4-mercaptopyridine (MCP), L,L-diphenylalanine, 1,1,1,3,3,3-hexafluoro-2-propanol (HFIP), 1-ethyl-3-(3-(dimethylamino)propyl) carbodiimide (EDC), *N*-hydroxysuccinimide (NHS), 1-pyrenebutyric acid 97%, and urease type III (EC. 3.5.1.5, from Jack Bean, 15.000−50.000 U g^{-1}) were obtained from Sigma-Aldrich (USA). With the exception of aniline, which was distilled prior to use, all reagents were used as received. All solutions were prepared using ultrapure water from a Milli-Q system (resistivity > 18 MΩ cm^{-1}).

2.2. Synthesis and Nanostructure Process. Fresh stock solutions were prepared by dissolving the lyophilized form of the peptide in HFIP at a concentration of 50 mg mL^{-1}. The peptide solution was then dropped on aluminum-coated glass substrates (50 μL) and spin coated at 1000 rpm for 30 s. The substrates that contained the films were placed on an elevated platform in an uncovered Petri dish that contained 20 mL of the appropriate solvent (isopropanol in our case) such that only the vapor reached the film. The entire setup was covered with aluminum foil and placed on a hot plate at 80 °C. The incubation time was 720 min, after which a layer of FF-MNSs was formed on the substrates. The FF-MNSs were used as the dielectric layer in OFETs.

FF-MNSs were functionalized in order to study enzyme−analyte interactions. A gold electrode was placed in a 100 mmol L^{-1} MCP solution for 2 h to coat the metallic surface with a thiol layer. Self-assembly of FF-MNSs was performed directly on the substrates using a variation of the solid−vapor-phase approach proposed by Ryu and Park.[19] This method was also detailed in a previous work.[20] Functionalization of FF-MNSs was achieved by drop coating 15 μL (7.0 mmol L^{-1}) of 1-pyrenebutanoic acid (PBA) in ethanol solution onto the FF-MNSs/MCP/Au electrode. The layer was then washed with water to remove the nonadsorbed PBA and dried at room temperature. For protein immobilization, 15 μL of a solution containing 30 mg mL^{-1} of urease (Urs) + 50 mmol L^{-1} of EDC + 50 mmol L^{-1} of NHS in a phosphate buffer with a pH of 6.5 (10 mmol L^{-1}) was cast with PBA-modified FF-MNSs/MCP/Au electrodes for 2 h at room temperature. Excess reagents were removed by washing with the phosphate buffer, and the electrode was tested immediately in an electrochemical cell.

2.3. Microscopy and Optical Spectroscopy. Scanning electron microscope (SEM) images were obtained using a JEOL FEG-SEM JSM 6330 F and a JEOL LV-SEM microscope at the Laboratory of Electron Microscopy of the Nanotechnology National Laboratory, Campinas, Brazil.

Raman spectra were collected by an Invia Renishaw spectrometer attached to a microscope with a × 50 lens. The system is equipped with two lasers, a 785 nm diode laser and a 514 nm argon ion laser.

2.4. Organic FET Fabrication. In order to prepare bottom-gate structures, we first thermally evaporate 60 nm of aluminum onto 1" × 1" organically cleaned glass microscope slides as the gate electrode. We fabricated both bulk FF devices (with no nanostructures) and devices with FF-MNSs as the dielectric layer. As discussed in section 2.2, FF-MNS films were deposited on Al-coated glass substrates. For the bulk FF films, the peptide compound was dissolved in HFIP (50 mg/mL) and spin coated on Al-coated glass substrates. The bulk FF films were left at room temperature in a nitrogen glovebox for a few hours before adding the pentacene layer on top. The thickness of the bulk FF dielectric layer is estimated to be ∼500 nm when using the accumulation capacitance of the MIS device and assuming a dielectric constant of 3.6.[9] This result was further confirmed by reflectometry. The thickness of the FF-MNS dielectric layer varied between 500 and 600 nm. Pentacene films (with 60 nm thickness) were thermally evaporated on top of bulk FF and FF-MNS layers, followed by thermal evaporation of a 40 nm thick layer of gold through a shadow mask containing both FET and capacitor structures for the top contacts.

Top-gate devices were prepared by depositing 40 nm of gold through a shadow mask onto 1" × 1" organically cleaned glass microscope slides. This was followed by thermal evaporation of 60 nm of pentacene. FF-MNSs were formed using identical spin-coating and nanostructure processes as in bottom-gate devices for the dielectric layer. This layer was thicker (∼800 nm) compared to the bottom-gate devices. A thin strip of aluminum was deposited through a shadow mask to a thickness of 60 nm on top of this dielectric layer to act as the gate electrode.

2.5. Electrical Characterization. The OFET characteristics were measured at room temperature with two source meters, Keithley 2400 and Keithley 236, configured together using a program written in LabVIEW. The source-drain current and source-gate leakage currents were measured with the Keithley 236, which has a resolution of 10 fA. Capacitance versus voltage characteristics were measured from both MIS and MIM structures with an HP 4284A LCR meter.

2.6. Electrochemical Measurements. Square-wave voltammetry (SWV) and electrochemical impedance spectra (EIS) were performed using a μAutolab Fra 2, Type III potentiostat/galvanostat. pH measurements were obtained with a Metrohm-Pensalab 827 pH

meter equipped with combined glass electrodes. All electrochemical measurements were performed in a conventional three-electrode electrochemical cell. The FF-MNSs/MCP/Au assembly was the working electrode (geometrical surface area = 0.07 cm^2), Pt wire was used as the auxiliary electrode, and a saturated calomel electrode (SCE) was used as the reference electrode. SWV assays were completed by applying a frequency of 50 Hz, a pulse amplitude of 70 mV, and a step potential of 2 mV vs SCE. The supporting electrolyte was a solution of 0.1 mol L^{-1} phosphate buffer solution (pH 6.2).

EIS was performed in the presence of 5 mmol L^{-1} $[Fe(CN)_6]^{3-/4-}$ and 0.1 mol L^{-1} KCl by applying an alternating current voltage with 5 mV amplitude in a frequency range from 1.0 Hz to 100 kHz. The electrolyte solution was purged with high-purity nitrogen for at least 15 min prior to each electrochemical experiment, and a nitrogen environment was then maintained for the solution in the cell during the measurement process.

3. RESULTS

3.1. Morphological Characterization. Since the performance of an OFET critically depends on the semiconductor–dielectric interface, high-resolution SEM images were obtained from neat FF-MNS films as well as from pentacene-deposited FF-MNS films. The growth conditions and substrates chosen for this study were identical to the OFET fabrication conditions. In order to minimize gate current leakage in the devices, the nonannealed FF-MNS film was deposited from a high concentration so as to form a dense network of nanostructures. Figure 1 shows SEM images of (a) annealed and (b) nonannealed FF-MNS films that were deposited on Al-coated glass substrates. In nonannealed FF-MNS films (Figure 1b), the self-assembly process may not be complete and there appears to be a resemblance to the amorphous phase. Upon annealing, clear micro/nanotape-like structures are seen in the SEM images (Figure 1a). Annealing of the films was carried out at 150 °C for 1 h, resulting in the orthorhombic phase. X-ray diffraction measurements from nonannealed and annealed FF-MNSs clearly show the two different phase formations: the hexagonal phase with $P6_1$ symmetry changes to an orthorhombic phase with $P22_12_1$ symmetry upon annealing.[20]

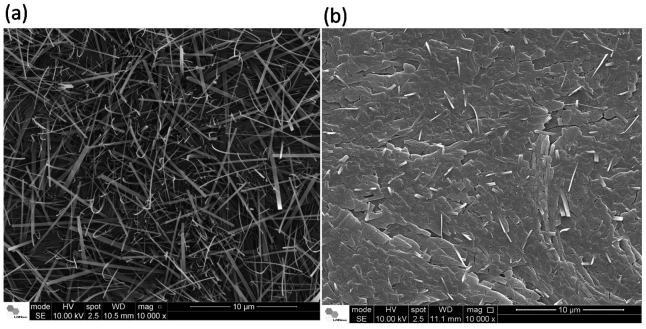

Figure 1. SEM images of (a) annealed and (b) nonannealed FF-MNS films. Isopropanol vapor was used to promote the nanostructuring of FF. (a) Film was annealed at 150 °C for 1 h.

Since pentacene was vacuum evaporated on top of the FF-MNS films in bottom-gate OFETs, we analyzed the morphology of these films in detail. Keeping in mind that the process of thermal deposition of the semiconductor layer can reach moderately high temperatures on the substrate and further promote penetration of the material into the underlying layer, Figure 2 gives us clues as to how the underlying FF-MNS film may be modified upon deposition of the pentacene film. The SEM image (top view) in Figure 2 is from an identical nonannealed FF-MNS film as the one shown in Figure 1b but with a thin film of pentacene (~60 nm) deposited on top. It clearly shows that the morphology of the FF layer changes compared to the nonannealed pristine film; there is formation of self-assembled structures upon which pentacene coats itself. The inset shows a section of the pentacene film where the FF-MNS layer was absent and the pentacene layer was grown on Al. Although typical dendritic features are not seen in the inset, the SEM image of pentacene grown on Al resembles growth of pentacene on other cross-linked polymer dielectrics.[17]

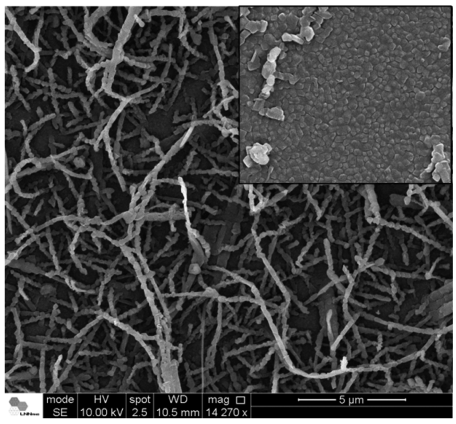

Figure 2. SEM image of a pentacene-coated nonannealed FF-MNS film grown on Al-coated glass. (Inset) Section of the pentacene film that was grown just on Al (with no FF-MNS layer underneath).

Our results thus indicate that the thermal energy during deposition of pentacene further promotes a nanostructuring effect in highly concentrated nonannealed FF-MNS films. Preliminary cross-sectional SEM images show a difference between the top layer (after pentacene was deposited) and the layers beneath it for nonannealed FF-MNSs; the nanostructuring effect is mainly seen at the surface, as shown in Figure S1, Supporting Information. A comparison of device performance with nonannealed FF-MNSs, annealed FF-MNSs, and bulk FF films (no nanostructures) provides some insight into the nature of the nanostructuring process, as discussed in section 3.5.

3.2. Raman Scattering Results—Annealed versus Nonannealed FF-MNS Films. Raman spectroscopy is a sensitive tool for probing self-assembly in biological macromolecules. For organic semiconductors this technique is particularly informative on chemical composition, segmental orientation, conformational distribution, and phase identification.[21] Both Raman and infrared (IR) signatures from FF nanostructures are well known[22,23] and can be used to determine the phase and other electronic effects (for functionalized tubes). The 1000 cm^{-1} Raman peak is the strongest in FF and FF-MNS, which arises from a ring deformation mode. There are clear differences between the Raman spectra of the annealed vs nonannealed films (Figure 3). New peaks are seen at 660 and 1507 cm^{-1} in the annealed sample. Also, the 1200 cm^{-1} region in the annealed FF-MNS sample shows additional Raman peaks. Due to a change in the structural symmetry of FF-MNSs from $P6_1$ in the hexagonal phase to $P22_12_1$ in the orthorhombic phase,[20] it is conceivable that silent Raman modes in the hexagonal phase become observable in the orthorhombic phase. The 1507 cm^{-1} peak is seen in FTIR; it is likely that this peak becomes Raman active in the orthorhombic phase. One could also apply such

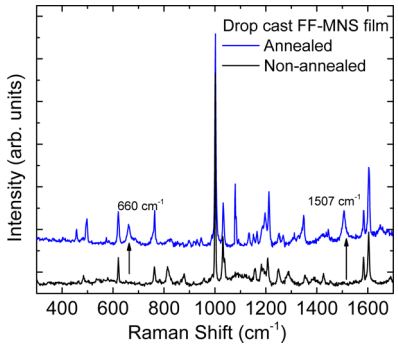

Figure 3. Raman spectra of nonannealed (black) and annealed (blue) FF-MNS film.

symmetry arguments to the 1200 cm^{-1} region, which mainly arise from C−H bending modes. However, full-scale ab initio calculations of the vibrational frequencies of the two phases of FF-MNSs are required to ascertain the exact origin of the peaks.

3.3. MIM Capacitors with FF-MNS—Capacitance versus Voltage. Prior to using FF-MNS films as a dielectric layer in OFETs and MIS diodes, MIM capacitors were fabricated by sandwiching the FF-MNS layer between Al and Au. For the orthorhombic phase, the FF-MNS film was first annealed at 150 °C for 1 h, after which Au electrodes were deposited. The thicknesses of the nonannealed and annealed films were 630 and 560 nm, respectively. These values were calculated from MIM capacitance measurements (Figure 4) using a dielectric constant of 3.6 for both nonannealed and annealed FF-MNS. Film thicknesses were further confirmed by a profilometer and a reflectometer, and they were found to be within 2% of the values determined from the capacitance measurements.

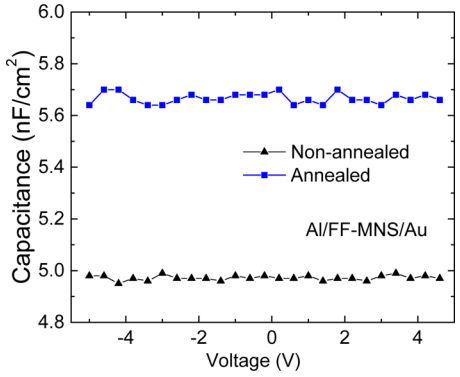

Figure 4. Capacitance vs voltage of MIM structures with nonannealed (black) and annealed (blue) FF-MNS films.

3.4. Pentacene OFETs with Bulk FF Film as the Dielectric Layer. As a prelude to using FF-MNS as a dielectric layer in an OFET, we wanted to make sure that the FF layer itself acts as a good dielectric layer. Bottom-gate structures using bulk FF film, as discussed in the Experimental Methods, were used.

Figure 5 shows the transfer and output characteristics; the inset of Figure 5a shows the capacitance−voltage characteristics of a pentacene MIS device with bulk FF as the dielectric layer. The charge carrier mobility is extracted using the standard saturation regime FET current−voltage (I−V) characteristics $\mu_{FET} = 2L/WC_0(\partial((I_{ds})^{1/2}/\partial V_g))^2$, where C_0 is the effective capacitance, W is the channel width, and L is the channel length of the transistor. V_g and I_{ds} are the gate voltage and source-drain current, respectively. The on−off ratio and charge carrier mobilities are 10^3 and 4×10^{-2} cm^2 V^{-1} s^{-1}, respectively. As discussed in the next section, these devices result in a catastrophic breakdown upon bias stress.

3.5. Pentacene OFETs with FF-MNS Film as the Dielectric Layer in Bottom-Gate Architecture. Both pentacene MIS and OFET devices were fabricated using FF-MNSs as the dielectric layer in a bottom-gate architecture. The FF-MNS layer was spin coated on Al-coated glass as discussed in the Experimental Methods. These micro/nanostructures were in the hexagonal phase, confirmed by Raman scattering. The inset of Figure 6a shows the capacitance vs voltage curve at 5 kHz from an MIS diode; a slight hysteresis is seen. The accumulation capacitance of 7.6 nF cm^{-2} is similar to what was seen for the bulk film, suggesting that the thicknesses of the dielectric layers are similar. The output characteristics (Figure 6b) show an increased modulation in output current compared to the bulk FF film-based OFET. Using the saturation region FET characteristics, the on−off ratio and charge carrier mobilities were determined to be 10^3 and 5.5×10^{-3} cm^2 V^{-1} s^{-1}, respectively.

The order of magnitude decrease in p-type charge carrier mobility with FF-MNSs compared with bulk FF film may be attributed to the morphology of pentacene. Due to the high surface roughness of the FF-MNS layer, the pentacene layer does not show its typical large dendritic features,[17] although the

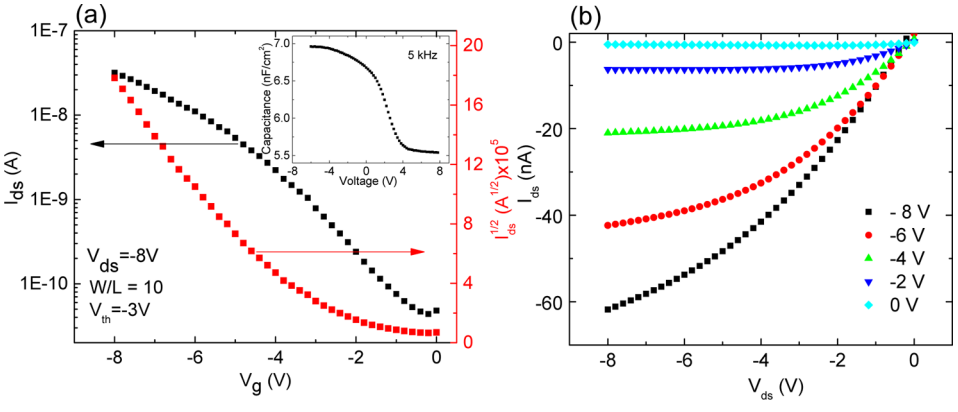

Figure 5. (a) Transfer and (b) output characteristics from pentacene OFETs using FF film as the dielectric layer. (Inset in a) Capacitance vs voltage characteristics at 5 kHz from an MIS structure.

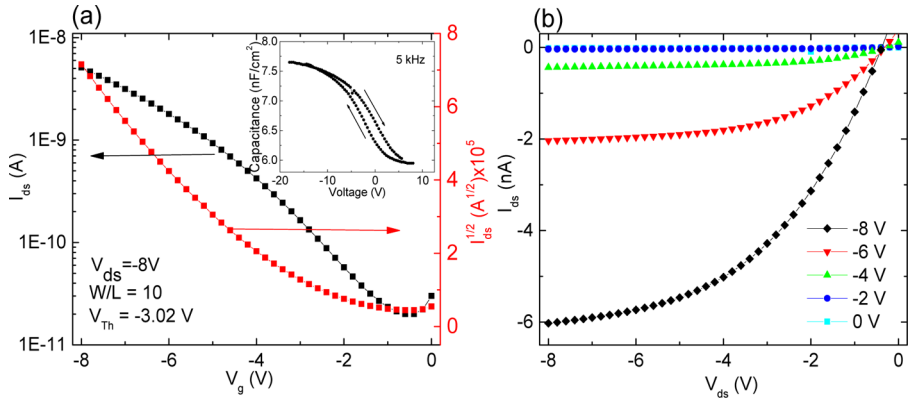

Figure 6. (a) Transfer and (b) output characteristics from pentacene OFETs using nonannealed FF-MNS as the dielectric layer. (Inset in a) Capacitance vs voltage characteristics at 5 kHz from an MIS structure.

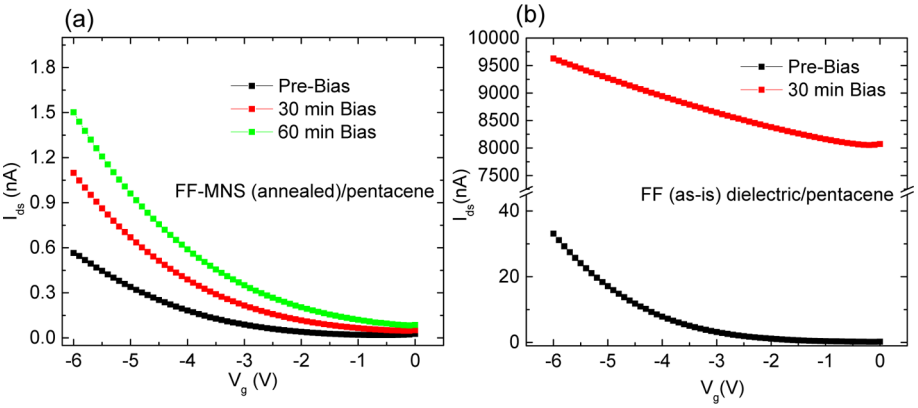

Figure 7. Operational stability of (a) annealed FF-MNS-based OFET and (b) bulk FF-based OFET. Transfer characteristics were measured after applying a bias of $V_g = V_{ds} = -6$ V for varying stress times.

crystalline nature of pentacene appears to be similar to pentacene films deposited on other substrates, as inferred from Raman scattering (Figure S2, Supporting Information). Annealing the FF-MNS layer such that it is in the orthorhombic phase does not improve the device performance in terms of carrier mobility and on−off ratios. There is a slight change in the thickness of the FF-MNS layer upon annealing, also seen in the MIM performance (Figure 4), which translates to a slightly higher leakage in the $I-V$ characteristics in pentacene OFETs. The gate leakage current was at least 1 order of magnitude lower than I_{ds} for all bottom-gate OFETs.

To investigate the bias stress effect in OFETs, which is typically manifested as a change in threshold voltage (V_{Th}) and/or hysteresis in the output current characteristics, we applied $V_g = V_{ds} = -6$ V for set times and the $I-V$ transfer characteristics were measured after each set. The OFETs were subjected to a total of 3600 s of bias stress. Figure 7a shows the transfer characteristics of an annealed FF-MNS/pentacene OFET. A shift of ∼0.5 V is observed in V_{Th} after 1 h of bias stress. Bias stress investigations with similar time scales on SiO_2-based pentacene OFETs typically show large V_{Th} shifts[24] and can be further correlated to structural changes.[25,26] Similar bias stress measurements were also conducted on pentacene OFETs using bulk FF as the dielectric layer (Figure 7b); surprisingly, after 30 min of bias stress the devices completely breakdown.

Although OFETs fabricated with bulk FF films perform slightly better than with FF-MNS films, it is clear from the bias stress analysis that FF nanostructures make the devices far more robust compared to bulk FF when subjected to a sustained electric field. Furthermore, bias stress measurements were also performed on nonannealed FF-MNS/pentacene OFETs. These devices did not perform as well as the annealed FF-MNS films but were better than the bulk FF devices. As seen in the SEM images (Figure 2), pentacene growth promotes a nanostructuring effect in nonannealed FF-MNS films. The bias stress results indicate that a significant portion of the bulk of the nonannealed FF-MNS film may not have the same nanoscale morphology as the surface, as is evident from Figure S1, Supporting Information. The above results clearly show that as long as FF is in the form of nanostructures they can withstand the force due to the applied electric field (∼10^5 V cm^{-1}) because of their larger surface area compared to bulk FF. For robust working devices, it is thus important that FF should be highly nanostructured, opening up several applications where one may use FF-MNSs as scaffolds for solution-processable conjugated polymers/oligomers to improve the stability and alignment preferences of the organic semiconductor itself.

3.6. Pentacene OFETs with FF-MNS Film as the Dielectric Layer in a Top-Gate Architecture. A large challenge lies in top-gate pentacene and other vacuum-evaporated organic semiconductor-based OFETs. In such structures, polymer dielectrics are typically used and the solvent incompatibility, especially with pentacene, is a major problem. Most organic solvents used for dissolving the polymer

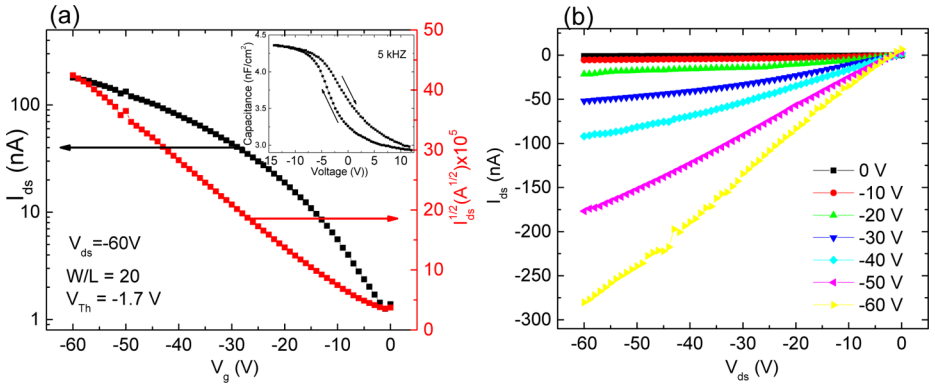

Figure 8. (a) Transfer and (b) output characteristics from top-gate FF-MNS-based pentacene. (Inset in a) Capacitance vs voltage characteristics at 5 kHz from an MIS structure.

dielectric damage the pentacene layer. There are a few reports of top-gate pentacene OFETs;[27−29] however, in most cases the gate dielectric is not simply spin coated on top of the pentacene layer but rather lift-off, lamination, or other techniques are used for incorporating the gate dielectric layer.

Figure 8 shows the transistor $I-V$ characteristics from top-gate pentacene OFETs with FF-MNSs as the dielectric layer. Higher operating voltage compared to bottom-gate architecture devices is most likely due to a higher thickness of the FF-MNS layer (~800 nm). The on−off ratio and charge carrier mobilities were determined as 10^2 and 2.5×10^{-3} cm^2 V^{-1} s^{-1}, respectively. We point out that all our measurements are performed in air, and even after a few days, the $I-V$ characteristics of both bottom-gate and top-gate devices do not degrade. Since the FF-MNS (mainly the hexagonal phase) layer is hydrophobic, the impact of air and moisture in such devices is minimal.

Organic FETs are being routinely used for biosensing applications.[30−32] The top-gate OFET architecture demonstrated above is a practical approach for applications in sensing, such as enzyme−analyte and antibody−antigen interactions. Functionalizing FF-MNSs is relatively straightforward and can be readily used in top-gate OFETs. In the next section we demonstrate a potential application of functionalized FF-MNSs in urease detection using electrochemical methods.

3.7. Functionalized FF-MNSs/MCP/Au Electrode and Enzyme−Analyte Detection. The assembly process of PBA onto FF-MNSs/MCP/Au electrodes has been monitored by electrochemical impedance spectroscopy (EIS). The aromatic pyrenyl moiety interacts with the aromatic-like structure of the FF-MNS walls through irreversible $\pi-\pi$ stacking at the FF-MNS and PBA interface.[33] The carboxylic acid functional groups from the PBA-modified FF-MNS surface were used for covalent coupling of complementary amino groups of urease (Urs). In this case, the carboxylic acid residues were functionalized to an active ester using carbodiimide and NHS reagents prior to coupling of the functionalized monolayer associated with the electrode to the protein.[34]

Figure 9 shows the impedance features of electrodes in the presence of equimolar $[Fe(CN)_6]^{3-/4-}$ at different steps of the functionalization process. Significant differences in the impedance spectra were observed during stepwise modification of the electrodes. To obtain more detailed information about the interfacial electrical properties between the electrodes and the electrolyte, the Randles circuit (inset of Figure 9) was chosen to fit the obtained impedance data.[35,36] In the Randles

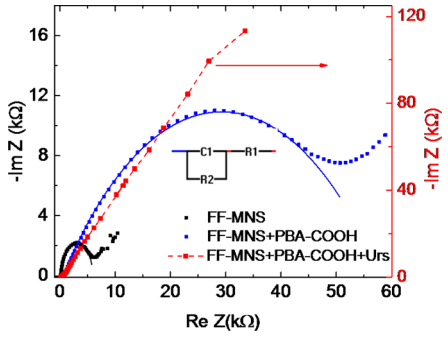

Figure 9. Electrochemical impedance spectroscopy for the different electrodes: FF-MNSs/MCP/Au (black), PBA/FF-MNSs/MCP/Au (blue), and Urs/PBA/FF-MNSs/MCP/Au (red) in 0.1 mol L^{-1} KCl containing 5 mmol L^{-1} $[Fe(CN)_6]^{3-/4-}$ as the probe. Solid lines are fit to the equivalent circuit shown in the inset.

circuit, it is assumed that the resistance for charge transfer (R_{et}), depicted as R_2, is parallel to the interfacial capacitance (C_1), giving rise to a semicircle in the complex plane plot of Z_{im} (imaginary part of the impedance) against Z_{re} (real part of the impedance). We note that in this circuit the diffusion impedance can be neglected. R_{et} for the FF-MNSs/MCP/Au electrode was estimated to be ~6 kΩ and increased to 60 kΩ when the electrode was modified with PBA; peripheral carboxylate groups, which produced negative charge, decrease the electron transfer for the $[Fe(CN)_6]^{3-/4-}$ molecules. It is also seen that the capacitance increases by almost a factor of 3 for the fully functionalized FF-MNSs, most likely due to the presence of an excess of negative charge generated on the surface, resulting in a pH change of the electrolyte solution (6.5) in comparison to the pK_{PB} = 4.8.[37] Furthermore, assembly of Urs on the functionalized electrode produced an insulating layer on the electrode surface that acts as a barrier to the interfacial electron transfer. This was reflected by an increase of R_{et} to over 200 kΩ. The results demonstrate that PBA and subsequently the protein, Urs, were successfully immobilized on the surface of modified electrode. SEM images of the electrode with FF-MNSs were measured before and after functionalization with PBA and Urs, as shown in Figure S3 (Supporting Information). Although the morphology of FF-MNSs remain unchanged, functionalized FF-MNSs show the presence of a polymeric film layer on the surface of the tubes, which can be assigned to PBA and Urs self-assembled arrays adsorbed preferentially along the longitudinal direction of the nanotubes.

Since the capacitance and R_{et} of FF-MNSs change significantly upon functionalization and further interaction with the protein (Urs), functionalized FF-MNSs may serve as an excellent dielectric in top-gate OFETs providing a simple device architecture for enzyme−protein detection. Such applications are currently being explored.

Examination of the performance of Urs/PBA/FF-MNSs/MCP/Au electrodes was carried out for different concentrations of Urs in a phosphate buffer solution (Figure 10) using

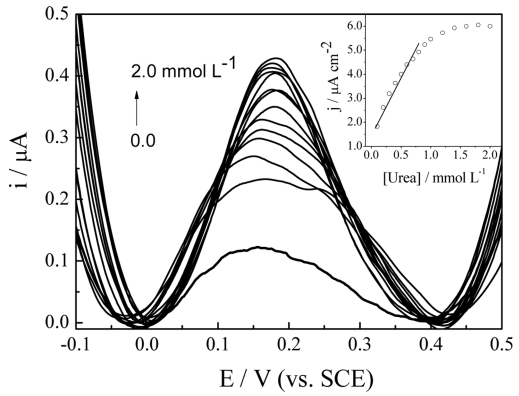

Figure 10. Square wave voltammetric evolutions of the Urs-PBA/FF-MNSs/MCP/Au electrode in 0.1 mol L^{-1} phosphate buffer solution containing different concentrations of Urs. (Inset) Plot of current density versus concentrations of Urs.

SWV. At Urs concentration greater than 0.9 mmol L^{-1}, the current response did not increase any further, a phenomenon usually attributed to saturation of the catalytic sites.

From the plot of the current response against concentration (inset Figure 10), a linear relationship was obtained for the concentration range of 0.1−0.8 mmol L^{-1}

$$j(\mu A\,cm^{-2}) = (4.57 \pm 0.36)[urea]/mmol\,L^{-1} + (1.64 \pm 0.16) \quad (R^2 = 0.96284)$$

The sensitivity was estimated as 4.57 ± 0.36 μA cm^{-2} $mmol^{-1}$ L, while the limit of detection (LOD = 3.3 s/m, where s is the relative standard deviation of the intercept and m is the slope of the linear current versus concentration of urea) was (0.15 ± 0.04) mmol L^{-1}. The LOD of our electrode was much lower and at about the same magnitude as values reported in the literature for other modified electrodes used for Urs electrocatalysis and detection.[38] These findings reveal a highly sensitive sensor capable of detecting urea even below the physiological levels of 1−100 mmol L^{-1}, typically observed in urine and blood samples.[39] In our case, the samples require dilution prior to analytical measurements, which is potentially advantageous because it allows for a finer control of sensing conditions. For example, by diluting the sample to low concentration levels, it is possible to accurately adjust the pH in solution and thus reduce the effect of interfering species.[40]

4. SUMMARY AND PROSPECT

Peptide nanostructures have great potential in organic electronics, either as scaffolds which can help align conjugated polymers/molecules or as active materials when functionalized. Our work reports for the first time the use of diphenylalanine peptide nanostructures as the gate dielectric in OFETs. We show that for OFETs to withstand a bias stress effect, the nanostructured morphology of the peptide layer is essential. FF-MNSs further allow a simple fabrication of top-gate pentacene OFETs, which could pave the way for enzyme−analyte sensing applications in the future. Using electrochemical methods we demonstrate that functionalized FF-MNSs are very sensitive in protein (Urs) detection. Electrochemical impedance spectroscopy shows that both interfacial capacitance and charge transfer resistance change significantly when the FF-MNS layer is functionalized with pyrenebutanoic acid and upon interaction with Urs. A second method using square wave voltammetry was also used to show the efficacy of FF-MNSs in Urs detection. Functionalized FF-MNSs in top-gate OFETs are thus a viable platform for future applications in protein−analyte detection.

Future improvement in OFET performance will be achieved by aligning the nanotube structures and reducing the thickness of the FF-MNS layer. This will greatly reduce the surface roughness and improve the interface between the conjugated molecule/polymer and the dielectric layer. Since many of the solvents used for dissolving organic semiconductors are orthogonal to the FF-MNS layer, pentacene may be easily replaced by other solution-processable conjugated polymers. The combination of FF-MNSs with organic semiconductors opens up a new generation of biocompatible materials in organic electronics.

■ ASSOCIATED CONTENT

Ⓢ Supporting Information

Cross-sectional SEM images of the pentacene/FF-MNS interface; Raman spectra of pentacene on FF-MNS and other dielectric layers; SEM images of FF-MNS-coated electrodes. This material is available free of charge via the Internet at http://pubs.acs.org.

■ AUTHOR INFORMATION

Corresponding Authors

*E-mail: wendel.alves@ufabc.edu.br.

*E-mail: guhas@missouri.edu.

Author Contributions

The manuscript was written through contributions of all authors. All authors have given approval to the final version of the manuscript.

Notes

The authors declare no competing financial interest.

■ ACKNOWLEDGMENTS

We acknowledge the support of this work through the U.S. National Science Foundation under Grant Nos. IIA-1339011 and ECCS-1305642. This work was also supported by FAPESP (grant nos. 2013/12997-0 and 2014/03813-5), INCT in Bioanalytics (FAPESP grant no. 08/57805-2 and CNPq grant no. 573672/2008-3), and CNPq (grant nos. 472197/2012-6 and 400239/2014-0). We thank Michelle Liberato for the cross-sectional SEM images.

■ REFERENCES

(1) Rosenman, G.; Beker, P.; Koren, I.; Yevnin, M.; Bank-Srour, B.; Mishina, E.; Semin, S. Bioinspired Peptide Nanotubes: Deposition Technology, Basic Physics and Nanotechnology Applications. *J. Pept. Sci.* **2011**, *17*, 75−87.

(2) Beker, P.; Rosenman, G. Bioinspired Nanostructural Peptide Materials for Supercapacitor Electrodes. *J. Mater. Res.* **2011**, *25*, 1661−1666.

(3) Stone, D. A.; Hsu, L.; Stupp, S. I. Self-Assembling Quinquethiophene−Oligopeptide Hydrogelators. *Soft Matter* **2009**, *5*, 1990.
(4) Hashemi, M.; Fojan, P.; Gurevich, L. The Many Faces of Diphenylalanine. *J. Self-Assem. Mol. Electron.* **2013**, *1*, 195−208.
(5) Liberato, M. S.; Kogikoski, S., Jr.; Silva, E. R.; Coutinho-Neto, M. D.; Scott, L. P.; Silva, R. H.; Oliveira, V. X., Jr.; Ando, R. A.; Alves, W. A. Self-Assembly of Arg-Phe Nanostructures via the Solid-Vapor Phase Method. *J. Phys. Chem. B* **2013**, *117*, 733−740.
(6) Souza, M. I.; Jaques, Y. M.; de Andrade, G. P.; Ribeiro, A. O.; da Silva, E. R.; Fileti, E. E.; Avilla Ede, S.; Pinheiro, M. V.; Krambrock, K.; Alves, W. A. Structural and Photophysical Properties of Peptide Micro/Nanotubes Functionalized with Hypericin. *J. Phys. Chem. B* **2013**, *117*, 2605−2614.
(7) Han, T. H.; Kim, J.; Park, J. S.; Park, C. B.; Ihee, H.; Kim, S. O. Liquid Crystalline Peptide Nanowires. *Adv. Mater.* **2007**, *19*, 3924−3927.
(8) Han, T. H.; Ok, T.; Kim, J.; Shin, D. O.; Ihee, H.; Lee, H.-S.; Kim, S. O. Bionanosphere Lithography via Hierarchical Peptide Self-Assembly of Aromatic Triphenylalanine. *Small* **2010**, *6*, 945−951.
(9) Bdikin, I.; Bystrov, V.; Kopyl, S.; Lopes, R. P. G.; Delgadillo, I.; Gracio, J.; Mishina, E.; Sigov, A.; Kholkin, A. L. Evidence of Ferroelectricity and Phase Transition in Pressed Diphenylalanine Peptide Nanotubes. *Appl. Phys. Lett.* **2012**, *100*, 043702.
(10) Heredia, A.; Bdikin, I.; Kopyl, S.; Mishina, E.; Semin, S.; Sigov, A.; German, K.; Bystrov, V.; Gracio, J.; Kholkin, A. L. Temperature-Driven Phase Transformation in Self-Assembled Diphenylalanine Peptide Nanotubes. *J. Phys. D: Appl. Phys.* **2010**, *43*, 462001.
(11) Amdursky, N.; Beker, P.; Koren, I.; Bank-Srour, B.; Mishina, E.; Semin, S.; Rasing, T.; Rosenberg, Y.; Barkay, Z.; Gazit, E.; Rosenman, G. Structural Transition in Peptide Nanotubes. *Biomacromolecules* **2011**, *12*, 1349−1354.
(12) Rogers, J. A.; Bao, Z.; Baldwin, K.; Dodabalapur, A.; Crone, B.; Raju, V. R.; Kuck, V.; Katz, H.; Amundson, K.; Ewing, J.; Drzaic, P. Paper-Like Electronic Displays: Large-Area Rubber-Stamped Plastic Sheets of Electronics and Microencapsulated Electrophoretic Inks. *Proc. Natl. Acad. Sci.* **2001**, *98*, 4835−4840.
(13) Sekitani, T.; Someya, T. Stretchable, Large-area Organic Electronics. *Adv. Mater.* **2010**, *22*, 2228−2246.
(14) Jang, Y.; Kim, D. H.; Park, Y. D.; Cho, J. H.; Hwang, M.; Cho, K. Low-Voltage and High-Field-Effect Mobility Organic Transistors with a Polymer Insulator. *Appl. Phys. Lett.* **2006**, *88*, 072101.
(15) Chua, L.-L.; Zaumseil, J.; Chang, J.-F.; Ou, E. C. W.; Ho, P. K. H.; Sirringhaus, H.; Friend, R. H. General Observation of N-Type Field-Effect Behaviour in Organic Semiconductors. *Nature* **2005**, *434*, 194−199.
(16) Ukah, N. B.; Granstrom, J.; Sanganna Gari, R. R.; King, G. M.; Guha, S. Low-Operating Voltage and Stable Organic Field-Effect Transistors with Poly (Methyl Methacrylate) Gate Dielectric Solution Deposited from a High Dipole Moment Solvent. *Appl. Phys. Lett.* **2011**, *99*, 243302.
(17) Ukah, N. B.; Senanayak, S. P.; Adil, D.; Knotts, G.; Granstrom, J.; Narayan, K. S.; Guha, S. Enhanced Mobility and Environmental Stability in all Organic Field-Effect Transistors: The Role of High Dipole Moment Solvent. *J. Polym. Sci., Part B: Polym. Phys.* **2013**, *51*, 1533−1542.
(18) Souza, M. I.; Silva, E. R.; Jaques, Y. M.; Ferreira, F. F.; Fileti, E. E.; Alves, W. A. The Role of Water and Structure on the Generation of Reactive Oxygen Species in Peptide/Hypericin Complexes. *J. Pept. Sci.* **2014**, *20*, 554−562.
(19) Ryu, J.; Park, C. B. High-Temperature Self-Assembly of Peptides into Vertically Well-Aligned Nanowires by Aniline Vapor. *Adv. Mater.* **2008**, *20*, 3754−3758.
(20) Bianchi, R. C.; Silva, E. R.; Dall'Antonia, L. H.; Ferreira, F. F.; Alves, W. A. A Non-Enzymatic Biosensor Based on Au Electrodes Modified with Peptide Self-Assemblies for Detecting Ammonia and Urea Oxidation. *Langmuir* **2014**, *30*, 11464−11473.
(21) Hsu, S. L., Raman spectroscopic studies of polymer structures. In *Raman Scattering in Materials Science*; Weber, W. H.; Merlin, R., Ed.; Springer-Verlag: New York, 2000; Chapter VIII, pp 369−445.
(22) Ravikumar, B.; Rajaram, R. K.; Ramakrishnan, V. Raman and IR Spectral Studies of L-Phenylalanine L-Phenylalaninium Dihydrogenphosphate and DL-Phenylalaninium Dihydrogenphosphate. *J. Raman Spectrosc.* **2006**, *37*, 597−605.
(23) Lekprasert, B.; Korolkov, V.; Falamas, A.; Chis, V.; Roberts, C. J.; Tendler, S. J. B.; Notingher, I. Investigations of the Supramolecular Structure of Individual Diphenylalanine Nano- and Microtubes by Polarized Raman Microspectroscopy. *Biomacromolecules* **2012**, *13*, 2181−2187.
(24) Zilker, S. J.; Detcheverry, C.; Cantatore, E.; de Leeuw, D. M. Bias Stress in Organic Thin-Film Transistors and Logic Gates. *Appl. Phys. Lett.* **2001**, *79*, 1124−1126.
(25) Adil, D.; Kanimozhi, C.; Ukah, N.; Paudel, K.; Patil, S.; Guha, S. Electrical and Optical Properties of Diketopyrrolopyrrole-Based Copolymer Interfaces in Thin Film Devices. *ACS Appl. Mater. Interfaces* **2011**, *3*, 1463−1471.
(26) Adil, D.; Guha, S. Surface-Enhanced Raman Spectroscopic Studies of Metal−Semiconductor Interfaces in Organic Field-Effect Transistors. *J. Phys. Chem. C* **2012**, *116*, 12779−12785.
(27) Kwon, T.; Baek, C.; Lee, H. H. Top Gate Pentacene Thin Film Transistor with Spin-coated Dielectric. *Org. Electron.* **2007**, *8*, 615−620.
(28) Onojima, N.; Takahashi, S.; Kato, T. Pentacene-based Organic Field-Effect Transistors with Poly(Methyl Methacrylate) Top-Gate Insulators Fabricated by Electrostatic Spray Deposition. *Synth. Met.* **2013**, *177*, 72−76.
(29) Zhang, L.; Di, C.-a.; Zhao, Y.; Guo, Y.; Sun, X.; Wen, Y.; Zhou, W.; Zhan, X.; Yu, G.; Liu, Y. Top-Gate Organic Thin-Film Transistors Constructed by a General Lamination Approach. *Adv. Mater.* **2010**, *22*, 3537−3541.
(30) Demelas, M.; Lai, S.; Spanu, A.; Martinoia, S.; Cosseddu, P.; Barbaro, M.; Bonfiglio, A. Charge Sensing by Organic Charge-Modulated Field Effect Transistors: Application to the Detection of Bio-Related Effects. *J. Mater. Chem. B* **2013**, *1*, 3811−3819.
(31) Rivnay, J.; Owens, R. M.; Malliaras, G. G. The Rise of Organic Bioelectronics. *Chem. Mater.* **2013**, *26*, 679−685.
(32) Berggren, M.; Richter-Dahlfors, A. Organic Bioelectronics. *Adv. Mater.* **2007**, *19*, 3201−3213.
(33) Martins, T. D.; de Souza, M. I.; Cunha, B. B.; Takahashi, P. M.; Ferreira, F. F.; Souza, J. A.; Fileti, E. E.; Alves, W. A. Influence of pH and Pyrenyl on the Structural and Morphological Control of Peptide Nanotubes. *J. Phys. Chem. C* **2011**, *115*, 7906−7913.
(34) Sousa, C. P.; Polo, A. S.; Torresi, R. M.; de Torresi, S. I. C.; Alves, W. A. Chemical Modification of a Nanocrystalline TiO2 Film for Efficient Electric Connection of Glucose Oxidase. *J. Colloid Interface Sci.* **2010**, *346*, 442−447.
(35) Bard, A. J.; Faulkner, L. R. *Electrochemical Methods: Fundamentals and Applications*, 2nd ed.; Wiley: New York, 2000.
(36) Sabatani, E.; Rubinstein, I.; Maoz, R.; Sagiv, J. Organized self-assembling Monolayers on Electrodes: Part I. Octadecyl Derivatives on Gold. *J. Electroanal. Chem. Interfacial Electrochem.* **1987**, *219*, 365−371.
(37) Tulock, J. J.; Blanchard, G. J. Role of Probe Molecule Structure in Sensing Solution Phase Interactions in Ternary Systems. *J. Phys. Chem. A* **2000**, *104*, 8340−8345.
(38) Srivastava, R. K.; Srivastava, S.; Narayanan, T. N.; Mahlotra, B. D.; Vajtai, R.; Ajayan, P. M.; Srivastava, A. Functionalized Multilayered Graphene Platform for Urea Sensor. *ACS Nano* **2011**, *6*, 168−175.
(39) Chen, J.-C.; Chou, J.-C.; Sun, T.-P.; Hsiung, S.-K. Portable Urea Biosensor Based on the Extended-gate Field Effect Transistor. *Sens. Actuators, B* **2003**, *91*, 180−186.
(40) Kovács, B.; Nagy, G.; Dombi, R.; Tóth, K. Optical Biosensor for Urea with Improved Response Time. *Biosens. Bioelectron.* **2003**, *18*, 111−118.